A8: Resonators
Semiconductor Physics I - Laboratory

Hassan Tanveer - 3735258, Simon Briesenick - 3712933
Experiment conducted on: May, 18th 2021

I. Abstract

We report on the pulsed laser deposition (PLD) of dielectric layer stacks for producing Bragg reflectors (BR) and Micro cavity (MC) structures. For this, we used YSZ and Al_2O_3 as deposition materials. Using Spectroscopic Ellipsometry (SE), we show that the layer thicknesses can be accurately controlled using PLD. Reflectivity spectra for both (BR and MC) are simulated and discussed for a wide range of incidence angles (i.e. in-plane wave vectors) using the optical constants obtained from the SE measurements. Most notably, the shift of the photonic band gap in both structures to shorter wavelengths is explained, as well as the energy dispersion and polarization splitting of the cavity mode in the resonator. Additionally, the Q factor of the MC is calculated to be $Q \cong 500$. Before presenting and discussing the results, we summarize important theoretical aspects of periodically arranged dielectric materials.

II. Introduction

Photonic crystals provide a wide range of applications, specifically for novel active and passive optical devices and systems [1]. A periodic array of carefully selected and designed dielectric media form photonic energy gaps (stop bands) analogous to electronic energy gaps in crystals, even at low numbers of layer stacks. They also already exist and can be investigated in nature. The wing scales in *Morpho* butterflies for example, or the chitin shells of copepods have been shown to consist of photonic crystals. Fig. 1 shows an example of a *Sapphirina metallina* copepod and the reflectivity spectrum of its shell. The reflectance value R under normal incidence is quite large in the near-UV region. Under oblique incidence however, the reflectivity shifts to shorter wavelengths, making the copepod almost invisible to predators.

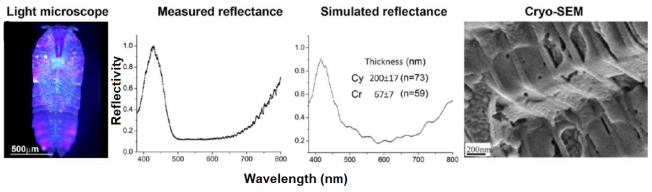

Fig. 1. The chitin shell of the male sapphirinid copepod consists of hexagonally packed layers, that can shift the reflectance spectrum into the UV spectrum under oblique angles of incidence. From [17].

A. Theoretical Background

1) Transfer matrix approach: The layered structures are modelled by a 2×2 transfer matrix formalism [2]. The transfer matrix $\hat{T}$ connects the electric field amplitudes $E^{\pm}_{a,s}$ travelling towards $(+)$ and away $(-)$ from the sample in the ambient (a) and in the substrate (s). For a single isotropic layer with refractive index n_i and layer thickness d_i, $\hat{T}_i$ is obtained using dynamical $\hat{D}_i$ and propagation matrices $\hat{P}_i$:

$$\hat{D}_i = \begin{cases} \begin{bmatrix} 1 & 1 \\ n_i\cos\theta_i & -n_i\cos\theta_i \end{bmatrix}, \text{ for TE waves} \\ \begin{bmatrix} \cos\theta_i & \cos\theta_i \\ n_i & -n_i \end{bmatrix}, \text{ for TM waves} \end{cases} \tag{1}$$

$$\hat{P}_i = \begin{bmatrix} e^{i\phi_i} & 0 \\ 0 & e^{-i\phi_i} \end{bmatrix}, \text{ with } \phi_i = k^i_\perp d_i \tag{2}$$

$$\hat{T}_i = \hat{D}_i\hat{P}_i\hat{D}_i^{-1} \tag{3}$$

$k^i_\perp$ is the perpendicular component of the wave vectors

$$k^i_\perp = \sqrt{\left(n_i\frac{\omega}{c}\right)^2 - (k^i_\parallel)^2} \tag{4}$$

and is related to the ray angle θ_i by

$$k^i_\perp = n_i\frac{\omega}{c}\cos\theta_i. \tag{5}$$

The energy of the photon is related to the vacuum wave vector k by

$$E = \hbar ck = \hbar c\sqrt{k^2_\perp + k^2_\parallel}. \tag{6}$$

For a multi-layer stack, this approach is repeated for each successive dielectric layer. The transfer matrix for an N-layer system is thus:

$$\hat{T} = \hat{D}_a^{-1}\left(\prod_{i=1}^{N}\hat{D}_i\hat{P}_i\hat{D}_i^{-1}\right)\hat{D}_s \tag{7}$$

Under the assumption, that the substrate as well as the ambient media are lossless, i.e. $n_{a,s}$ being real, the Reflectance R and Transmittance T are then

$$R = |r|^2 = \left|\frac{T_{21}}{T_{11}}\right|^2 \tag{8}$$

$$T = \frac{n_s\cos\theta_s}{n_a\cos\theta_a}|t|^2 = \frac{n_s\cos\theta_s}{n_a\cos\theta_a}\left|\frac{1}{T_{11}}\right|^2 \tag{9}$$

where r and t are the Fresnel coefficients and T_{ij} are the transfer matrix entries. In general for a multi-layer system, the matrix multiplication has to be performed by a computer. However, under normal incidence and for the layer stacks considered in this report, the matrices in eqns. (1) & (2) take algebraically simple forms and the matrix products can easily be calculated. These are presented in the following.

2) Bragg Mirrors: A Bragg mirror consists of N pairs of alternating quarter-waves

$$n_1 d_1 = n_2 d_2 = \frac{\lambda_0}{4} = \frac{\pi}{2}\frac{c}{\omega_0}, \tag{10}$$

where λ_0 is the centre of the stop-band of the mirror.

According to Eq. (3), the transfer matrix for the film stack is then given by

$$\hat{T} = \hat{D}_a^{-1}[\hat{D}_1\hat{P}_1\hat{D}_1^{-1}\hat{D}_2\hat{P}_2\hat{D}_2^{-1}]^N\hat{D}_s. \tag{11}$$

The transfer matrix across one layer is given for all wavelengths at normal incidence as

$$\hat{T}_j = \begin{bmatrix} \cos k_j d_j & \frac{i}{n_j}\sin k_j d_j \\ i n_j \sin k_j d_j & \cos k_j d_j \end{bmatrix} \tag{12}$$

where $j = 1, 2$. The transfer matrix product $\hat{T}_1\hat{T}_2$ that links the electric field amplitudes separated by a unit cell of width $\Lambda = d_1 + d_2$ can be used to obtain the stop band width analogous to the electronic band gap in crystals. According to the Bloch theorem, the electric field amplitudes in neighbouring unit cells differ by a constant phase factor. Hence, the effect of the transfer matrix $\hat{T}_1\hat{T}_2$ must be to multiply the electromagnetic wave amplitudes by said phase factor

$$\hat{T}_1\hat{T}_2\mathbf{E}(z) = e^{iK\Lambda}\mathbf{E}(z) \tag{13}$$

where $K \in \mathbb{C}$ is the Bloch wave number. Thus, $e^{iK\Lambda}$ is an eigenvalue of the transfer matrix product. To obtain the dispersion relation for K, the equation

$$\det\left(\hat{T}_1\hat{T}_2 - e^{iK\Lambda}\mathbb{1}\right) = 0 \tag{14}$$

needs to be solved. One obtains,

$$\cos K\Lambda = (T_{11} + T_{22})/2 \tag{15}$$

where T_{ii} are the components of the matrix product and are frequency dependant (since $k_j = n_j\frac{\omega}{c}$). Allowed photonic bands are those for which the RHS is bounded by

$$|(T_{11} + T_{22})/2| \leq 1, \tag{16}$$

for which the Bloch wave number is purely real and the electromagnetic wave experiences no attenuation while propagating through the material. Similarly, forbidden photonic bands are defined by

$$|(T_{11} + T_{22})/2| > 1, \tag{17}$$

for which Q has a non-zero imaginary part determining the decay of the electromagnetic wave that propagates through the crystal [3]. We will now discuss the effect of the Bragg mirror on light with wavelength λ_0 at normal incidence . The propagation matrix is then simply ($\phi_i = \pi/2$)

$$\hat{P}_{1,2} = \begin{bmatrix} i & 0 \\ 0 & -i \end{bmatrix}. \tag{18}$$

Carrying out the matrix multiplication,

$$\hat{D}_1\hat{P}_1\hat{D}_1^{-1}\hat{D}_2\hat{P}_2\hat{D}_2^{-1} = \begin{bmatrix} -n_2/n_1 & 0 \\ 0 & -n_1/n_2 \end{bmatrix} \tag{19}$$

and the reflectance in the central range of the stop band is thus

$$R = \left(\frac{n_a - \frac{n_1^2}{n_s}\left(\frac{n_1}{n_2}\right)^{2N-1}}{n_a + \frac{n_1^2}{n_s}\left(\frac{n_1}{n_2}\right)^{2N-1}}\right)^2 \tag{20}$$

for an odd number of layers $2N - 1$. In the vicinity of λ_0, the transfer matrix $\hat{T} = \hat{T}_1\hat{T}_2$ of a single unit cell can be approximated such that each entry is left only in linear terms in

$$x = (\omega - \omega_0)\frac{\lambda_0}{4c} \tag{21}$$

which leaves $\hat{T}$ as

$$\hat{T} = -\begin{bmatrix} \frac{n_2}{n_1} & i\left(\frac{1}{n_1} + \frac{1}{n_2}\right)x \\ i(n_1 + n_2)x & \frac{n_1}{n_2} \end{bmatrix}. \tag{22}$$

It can then be shown, that the (complex) reflection coefficient in the vicinity of ω_0 can then be written with the use of eqn. 20 as

$$r_{\text{DBR}} = \sqrt{R}e^{iL_{\text{DBR}}\frac{n_s}{c}(\omega-\omega_0)}. \tag{23}$$

Here, L_{DBR} is the *effective* length of the Bragg mirror and is a measure for the penetration depth of the field into the structure. It is given by [3]

$$L_{\text{DBR}} = \frac{n_1 n_2 \lambda_0}{2(n_2 - n_1)}. \tag{24}$$

To calculate the band width, a second-order expansion in x for $\hat{T}$ is needed. It can be approximated as [2]:

$$\Delta\lambda = \lambda_0\frac{2}{\pi}\frac{\Delta n}{n}, \tag{25}$$

where $\Delta n = |n_2 - n_1|$ and $n = 1/2(n_1 + n_2)$.

Under oblique incidence, the situation is generally more complex and needs to be evaluated for both s and p polarization states. Indeed, the reflection coefficient in eqn. 23 can still be used, however, the effective length of the Bragg mirror L_{DBR} as well as the reflectance R and the central frequency ω_0 need to be replaced with their respective values for s and p polarization (Can be found in [3]). In general, these quantities for the two polarization states are relatively close to each other and their differences can usually be disregarded. As the incident angle is increased, the central wavelength λ_0 shifts towards lower values. Indeed, it can be shown that the *effective* central wavelength is defined by [1]

$$\lambda_0' = \lambda_0\left(1 - \sin^2\theta/n_{\text{eff}}^2\right)^{1/2}. \tag{26}$$

n_{eff} is the effective refractive index, determined by an effective medium approach.

3) Microresonator: If the N-layer Quarter-Wave stack is modified, by inserting another Quarter-Wave layer in between the alternating high- and low-refractive index layer pairs, the resulting *cavity* is just a Half-Wave layer. A so-called latent layer satisfies the condition that $n_l d_l = \lambda_0/2$. Since that layer can fit exactly half of the reference wavelength (or integer multiples m of it) it has no optical effects and can be disregarded in the matrix product [4]. Then eqn. 7 can be simplified: The propagation matrix associated with the latent layer is simply a unit matrix or its negative. The product $\hat{D}_l \hat{P}_l \hat{D}_l^{-1}$ also becomes a unit matrix or its negative. Since the neighbouring layers are two Quarter-Wave layers of identical refractive indexes, they again form a latent layer and the process can be continued. Hence, the reflection and transmission coefficients at the reference wavelength is identical to that of the ambient-substrate interface only. A defect mode in the centre of the photonic band gap is introduced, a so-called cavity mode. Qualitatively, the situation is very similar to that of a standard Fabry-Pérot interferometer with planar mirrors and many of the results for the Fabry-Pérot interferometer also apply for the microcavity. However, due to the penetration of the cavity field into the Bragg mirrors on either side, the Fabry-Pérot cavity length needs to be replaced by the effective length:

$$L_{\text{eff}} = d_l + L_{\text{DBR}} \tag{27}$$

The cavity mode wave vector component perpendicular to the dielectric layers $k_\perp$, i.e. parallel to the plane normals is hence quantized as

$$k_\perp = \frac{m\pi}{d_l} = n_l \frac{\omega_l}{c}. \tag{28}$$

ω_l is the classical Fabry-Pérot freqency defined by the length of the cavity. The cavity mode then has an energy dispersion as

$$E_{\text{cav}} = \frac{\hbar c}{n_{\text{eff}}} \sqrt{k_\perp^2 + k_\parallel^2} \tag{29}$$

where n_{eff} is the effective refractive index of the layer stack. The mode frequency ω_{m} for a microcavity is given by [5]

$$\omega_{\text{m}} = \frac{d_l \omega_l + L_{\text{DBR}} \omega_0}{L_{\text{eff}}}, \tag{30}$$

where ω_0 is the central frequency in the stop band of the Bragg mirrors (assumed to be identical, a more general equation that takes into account different L_{DBR} and ω_0 for the two neighbouring mirrors can be found in [14]).

If the angle of incidence θ is now varied, $k_\parallel$ changes accordingly by

$$k_\parallel(\theta) = \frac{E}{\hbar c} \sin\theta \tag{31}$$

The Quality-factor of a resonator is defined by [3]:

$$Q = \frac{\lambda}{\Delta\lambda} \tag{32}$$

and gives a measure for the average number of times a photon of the reference wavelength is travelling back and fourth between the two mirrors before it escapes [6].

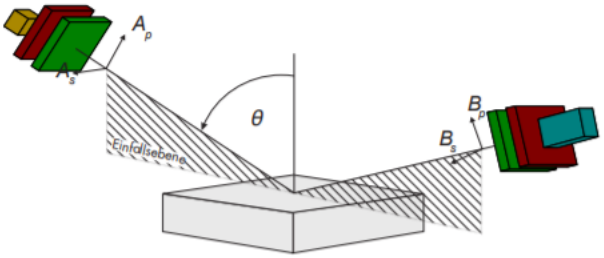

Fig. 2. Measurement setup: The $M2000$, From [7]

B. Experimental Setup

SE measurements were performed with the $M2000$ ellipsometer (see Fig. (2)) in the spectral range between 0.7 and $3.3eV$. Due to the limited spectral resolution of the rotating compensator $M2000$ spectrometer, additional SE data was acquired by the Variable Angle Spectroscopic Ellipsometer (VASE) for the Microresonator.

Ellipsometry is an optical technique that measures the change in polarization of the interacting light after being reflected from the sample. The ratio of the two (complex) reflection coefficients r_s (component perpendicular) and r_p (component parallel to the plane of incidence) is captured by the ellipsometric angles Δ and Ψ:

$$\frac{r_p}{r_s} = \tan\Psi \exp(i\Delta). \tag{33}$$

Hence, Ψ reflects the real part, while Δ records the imaginary part of the ratio. To fit the results to the theoretical predictions of the layer-stack model resulting from the above described transfer matrix approach, a set of parameters, like the layer thickness and optical parameters of each layer are varied. For the multi-layer stack, a transfer-matrix approach as described above leads to models for the optical constants. From these models, the layer thicknesses of the individual layers can be inferred. The software *Complete Ease* was used to implement such models and to obtain the ellipsometric data with corresponding fit models. All Figures containing experimental data are plots generated using *Python*.

C. Material Information

Three types of probes were investigated (see Fig. (4)):

1) Two multi-layer structures *MSF1125* and *MSF1126* (see Fig. (3a, 3b))
2) A YSZ/Al_2O_3 Bragg reflector (BR) with 10.5 layer pairs and
3) a Microresonators with a $\lambda/2-YSZ$ cavity between two BR with 10 layer pairs (*passive* resonator)

The used materials for the different layers are yttria-stabilized zirconia (YSZ) and alumina (Al_2O_3), grown by pulsed-laser deposition (PLD). According to [8] [9], PLD grown YSZ is typically found in a cubic structure and is transparent for a relatively large region from the near-infrared

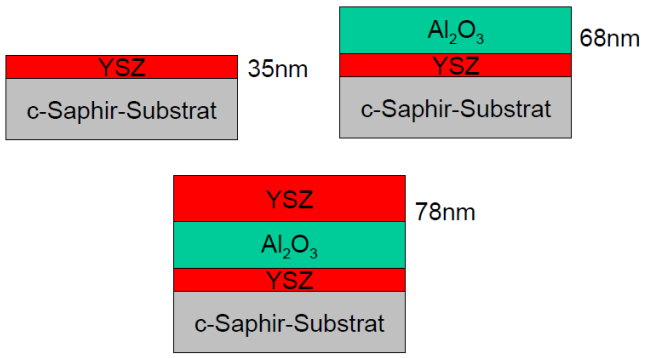

(a) MSF1125

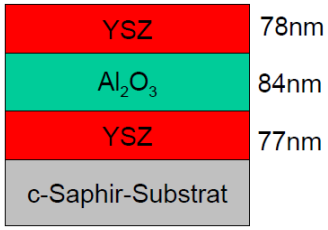

(b) MSF1126

Fig. 3. layer deposition for the two multilayer structures

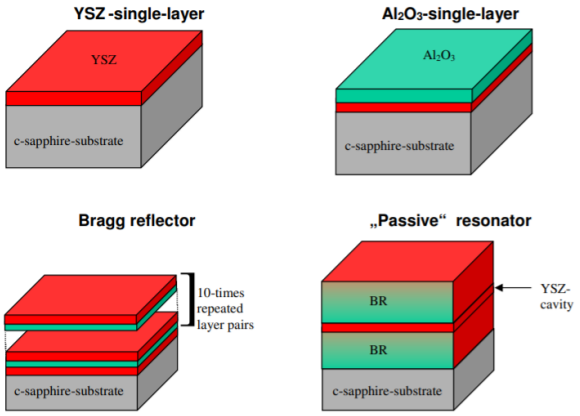

Fig. 4. Sample structures

(NIR) to the ultraviolet (UV). The optical band gap of YSZ is around $E_g = 5.7eV$.

PLD-sputtered Al_2O_3 films on the other hand typically grow in an amorphous structure [10] with a band gap energy of $E_g = 9.9eV$ [11]. As YSZ and Al_2O_3 are transparent dielectrics, the Cauchy Ansatz for the refractive index and the extinction coefficient was used:

$$n(E) = A + BE^2 + CE^4 \text{ and } k = 0. \tag{34}$$

A, B, and C are the Cauchy parameters and E is the energy of light.

1) Sample Preparation: All samples were grown using pulsed laser deposition (PLD). A pulsed KrF laser ($\lambda = 248nm$) with pulse energy of $600mJ$ and duration of $25ns$ is being absorbed by the target material on an area of roughly $3mm^2$ in the deposition chamber. A plasma plume emerges and hits the rotating sample (rotation of $1.5cpm$ $(0.03Hz)$). The substrate temperature during the deposition was held constant at $T \approx 650°C$. The oxygen pressure in the chamber during the deposition of the YSZ layers was at $p(O_2) = 2 \times 10^{-2}mbar$ and at $p(O_2) = 2 \times 10^{-3}mbar$ for the Al_2O_3 layers.

The layer-per-layer deposition process of the multi-layer structure is shown in Fig. (3a) for the *MSF1125* and in Fig. (3b) for the *MSF1126*.

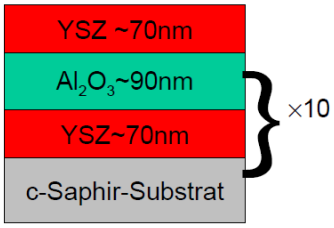

Fig. 5. layer deposition for the Bragg reflector

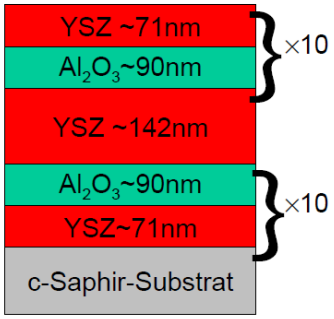

Fig. 6. layer deposition for the Microresonator

III. Results and Discussion

A. single layer YSZ on a c-sapphire substrate

As mentioned above, YSZ is isotropic and transparent and we can use a Cauchy model for the refractive index n with Cauchy paramters $A = 2.121$, $B = 0.01793$ eV^{-2} and $C = 0.00048806$ eV^{-4}. The model gives a layer thickness of $d = 35.38 \pm 0.02$nm which is in excellent agreement to the needed layer thickness for further processing of the *MSF1125*. Ψ and Δ for the single layer with additional models are given in Fig. 7a and 7b, respectively.

The behaviour of both quantities is largely determined by the Brewster angle and we would like to point to the discussion to our previous report [12] for more detail.

B. Al_2O_3 on YSZ layer

The alumina film was then sputtered onto the sample and subsequently measured in the ellipsometer. This approach has the advantage that the optical constants and the layer thickness of each film can be determined and fixed in the analysis of further films sputtered onto the sample. Since Al_2O_3 grows in

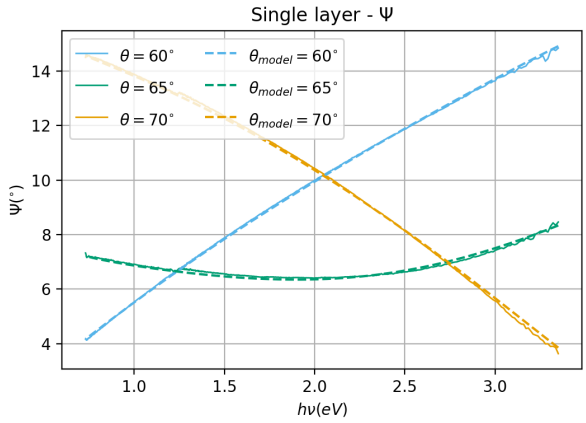

(a) Ψ vs. energy

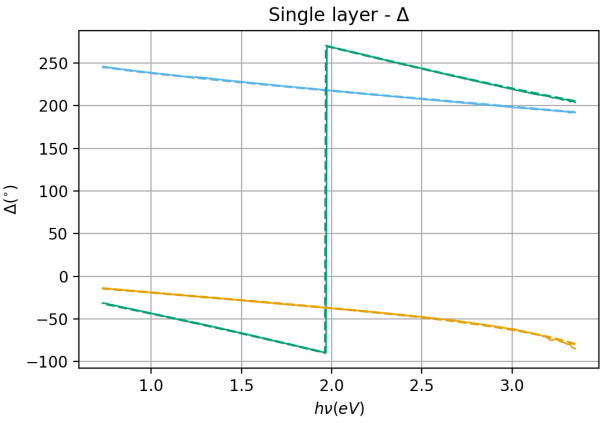

(b) Δ vs. energy

Fig. 7. $YSZ-$ single layer on substrate: Ψ and Δ for different incident angles θ (solid lines) and calculated corresponding models (dashed lines).

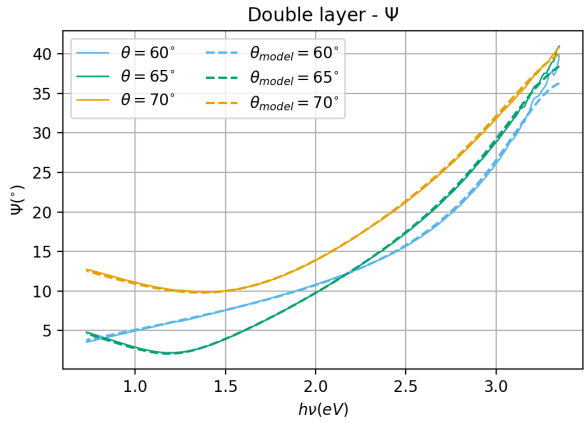

(a) Ψ vs. Energy

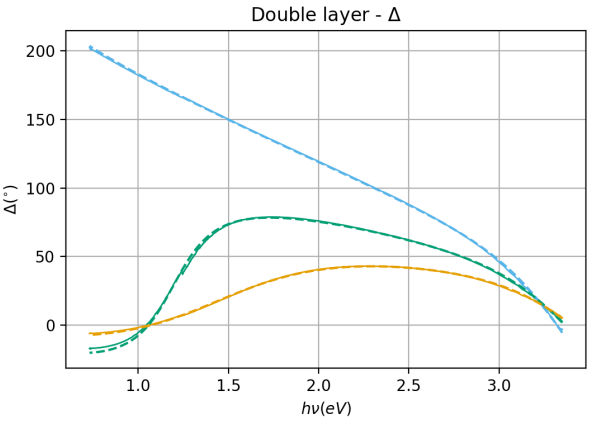

(b) Δ vs. Energy

Fig. 8. Double-layer structure: Ψ for different θ (solid lines) and corresponding models (dashed lines)

an amorphous structure and has a large band gap, a Cauchy model for fitting the optical constants can again be used (Here, $A = 1.713$, $B = 0.00309$ eV^{-2} and $C = 0$ eV^{-4}). Again, the layer thickness is a close match to the expected result, $d = 67.71 \pm 0.1$ nm with relative error $\delta_r < 0.5\%$.

C. S1125 and S1126 multilayer structures

Subsequently, a second YSZ layer was deposited onto the sample. After the deposition process, the top material will not be completely smooth in general. Instead, inhomogeneous crystal growth rate across the sample, as well as thermodynamic relaxation of the material species into energetically more favourable configurations are some of many important contributions against smooth surfaces on samples. In the effective medium approximation, an additional layer is assumed to be present on the samples. This additional layer differs from others - One assumes that the top material consists to some part of the same material as the top layer and to some part of air. In our case, we took the mixing ratio between these two to be 1:1. For both samples, the determined layer thickness was still relatively close to $d = 78$ nm with relative errors $\delta_{r,1125} < 0.2\%$ and $\delta_{r,1126} < 4\%$. Since the deposition processes should yield the same layer thicknesses, $\delta_{r,1125}$ is only coincidentally this close to the expected value.

D. Bragg Reflector

For the Bragg reflector with 10.5 layer pairs, (Ψ, Δ) are shown below. In the range of the stop band of the BR, the reflectivity ratio R_p/R_s is very close to unity and hence Ψ reaches almost 45°. Above and below the stop band, interference effects for the p and s polarized states cause oscillations. From the model fit for (Ψ, Δ), the layer thicknesses of the Bragg mirror layers are

$$d_{YSZ} = 75 \pm 0.4nm \tag{35}$$

$$d_{Al_2O_3} = 91.7 \pm 0.5nm \tag{36}$$

which corresponds to a central wavelength at normal incidence of $\lambda_0 = 4n_{YSZ}d_{YSZ} = 4n_{Al_2O_3}d_{Al_2O_3}$. Averaging the two results and converting to eV:

$$E_0(\theta = 0) = \frac{hc}{\lambda_0} = 1.90 \pm 0.1\text{eV}. \tag{37}$$

The simulated reflectivity for various angles of incidence is shown in Fig. 12. We can observe that the stop band position shifts to shorter wavelengths as the angle of incidence is

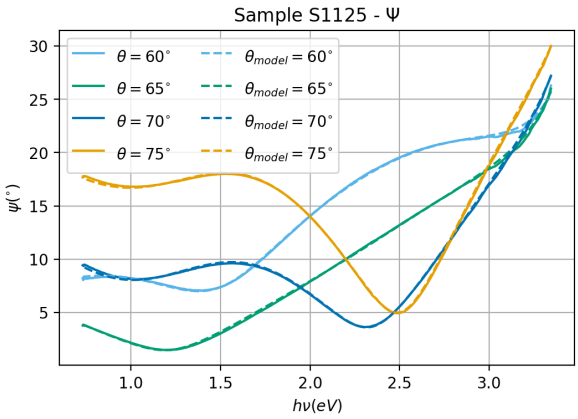

(a) Ψ vs. Energy

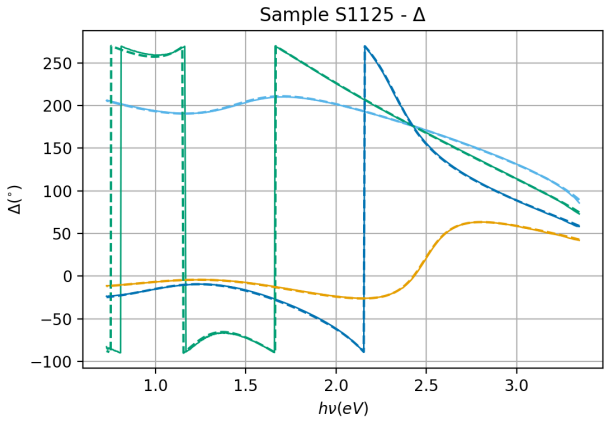

(b) Δ vs. Energy

Fig. 9. (Ψ, Δ) for the Multilayer structure S1125

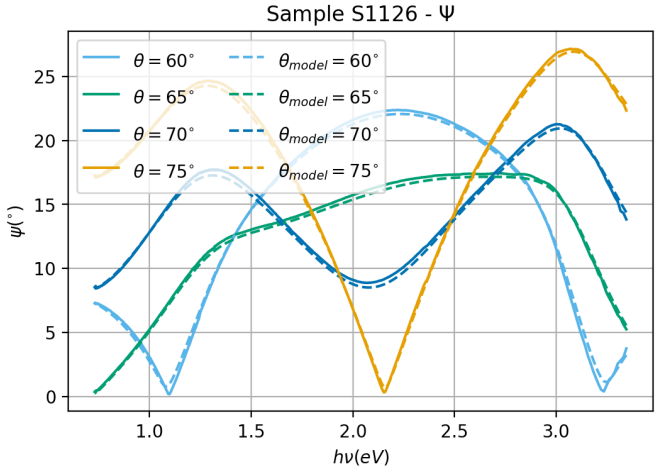

Fig. 10. (Ψ, Δ) for the Multilayer structure S1126

increased, as predicted in eqn. 26. The penetration depth at the central wavelength can be calculated from 24. With $n_1 = 1.73$, $n_2 = 2.22$ and $\lambda_0 = 650nm$, we obtained $L_{\text{DBR}} \sim 2500nm$ which corresponds to $\sim$ 16 layer pairs. This effect is also observable in the measured reflectivity spectrum, that was recorded using the reflectivity mode of

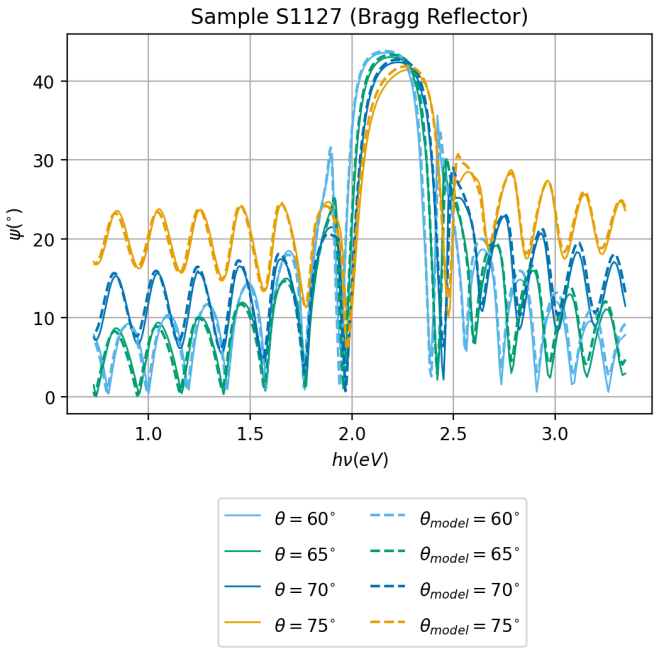

(a)

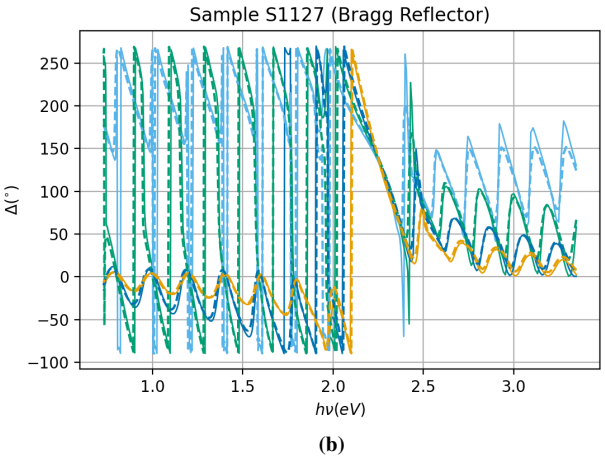

(b)

Fig. 11. (Ψ, Δ) for the Bragg reflector

the ellipsometer (Fig. 13). However, R in the stop-band does not reach it's theoretical value of close to unity.

E. Microresonator

The ellipsometric angles were recorded for four different angles of incidence between $60°$ and $75°$ (see Fig. 14). The deviation of the fit models to the data can be traced back to the measurement errors in the optical constants of each layer. Indeed, for example, this error propagation causes Δ to retain little of it's derivative-like structure at the band edges and has a much smother transition. As pointed out in [3] electron-beam evaporation is generally preferred for producing high quality and smooth, dielectric oxides. Nonetheless, the fit describes the data relatively well and is quite typical for Microresonator structures (compare for example with [13]). The layer thicknesses for the neighbouring Bragg mirrors are

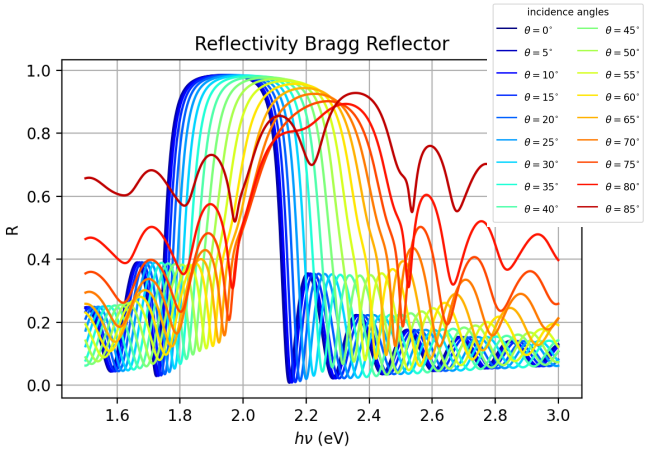

Fig. 12. Simulated Reflectivity for the Bragg reflector.

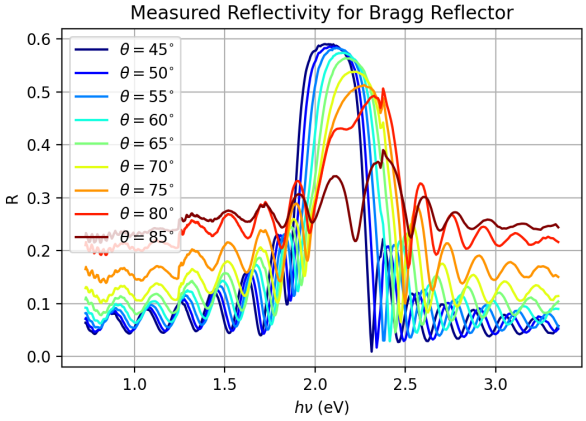

Fig. 13. In reflectivity mode, the reflectance of the BR only reaches $R \approx 0.6$ in the stop band region.

relatively close to those in the above given models. However, the cavity layer thickness in this fit shows large deviations. Instead of 142 nm, we could measure about $d_l = 153.7 \pm 0.2$ nm.

The microresonator reflectivity spectrum was recorded for angles of incidence between $0°$ and $85°$ and is shown in Fig. 15 for four equally spaced positions of the ellipsometer arms. The cavity peak positions can be seen to vary non-linearly with θ. Furthermore, a splitting for the two polarizations of light of the cavity energy can be observed at $\theta = 30°$ and above. The physical reason behind this splitting phenomena at oblique incidence lies in the nature of the Bragg mirrors that neighbour the cavity layer. As mentioned above, the effective length of the Bragg mirror L_{DBR}, as well as the central frequency ω_0 differ for the two polarization states. This leads to two different dispersions for the cavity energy and the photon lifetime. Indeed, referring to eqn. 30 the parameters L_{DBR} and ω_0 are dependant on the polarization states as mentioned in Sect. II B. The energy splitting is known as TE-TM splitting and an approximate equation for the difference between the two energies is given by [14]

$$\Delta E_{\text{TE-TM}} \propto (-\pi\hbar c + DE_0(\theta))(L_{\mathrm{DBR}}^{\mathrm{TE}} - L_{\mathrm{DBR}}^{\mathrm{TM}}). \qquad (38)$$

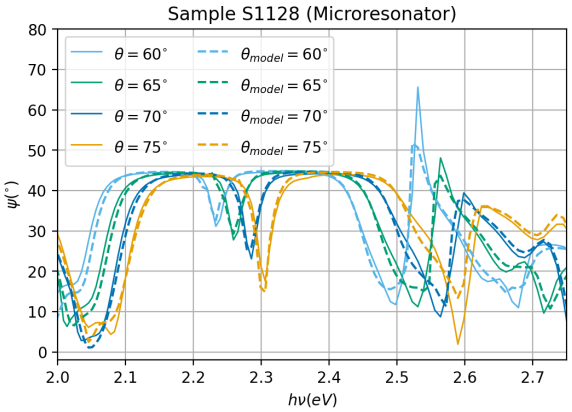

(a) Ψ vs. Energy

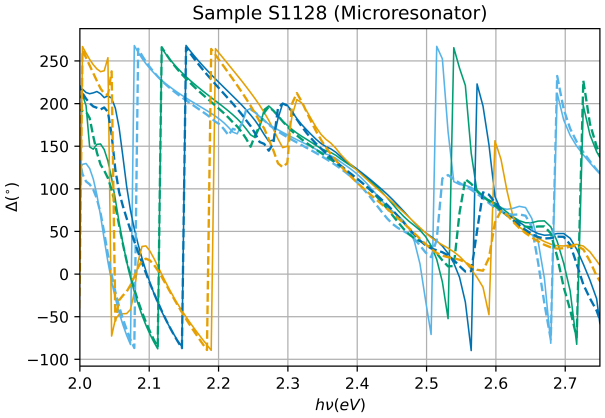

(b) Δ vs. Energy

Fig. 14. Microresonator: (Ψ, Δ) in the stop band region.

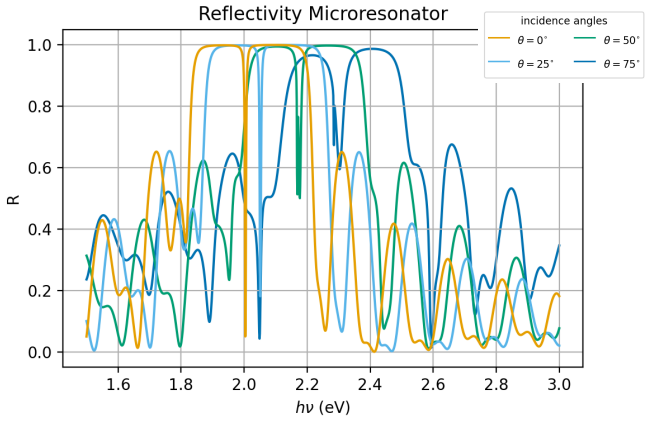

Fig. 15. Simulated Reflectivity for the Microresonator. For clarity, only 4 different angles of incidence are shown.

where D is given as

$$D = d_l n_l \sqrt{1 - \left(\frac{n_{Al_2O_3}}{n_l} \sin\theta_{Al_2O_3}\right)^2} \qquad (39)$$

and is dependant on the parameters $(n_{Al_2O_3}, \theta_{Al_2O_3})$ of the alumina film neighbouring the cavity layer. The last term is negative in our case as is the first, since $d_l \geq \pi\hbar c/n_l E_0 =$

$146nm$. Hence, the splitting will always be positive and the higher energy peak can be identified as corresponding to TE-polarized light.

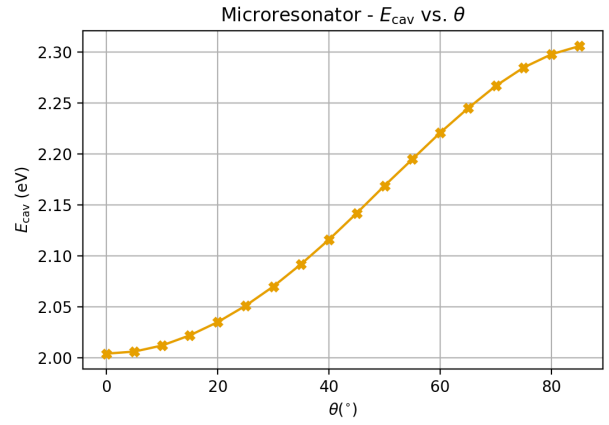

(a)

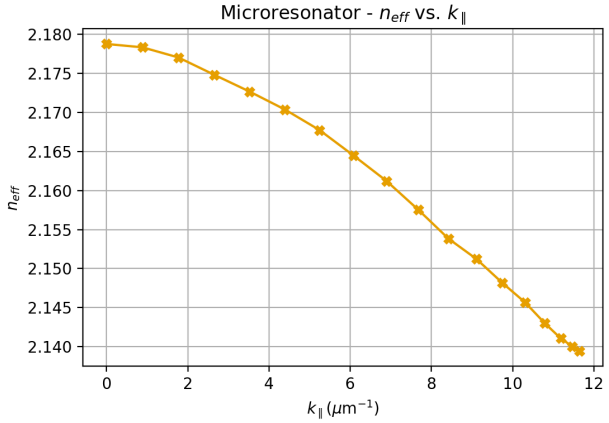

(b)

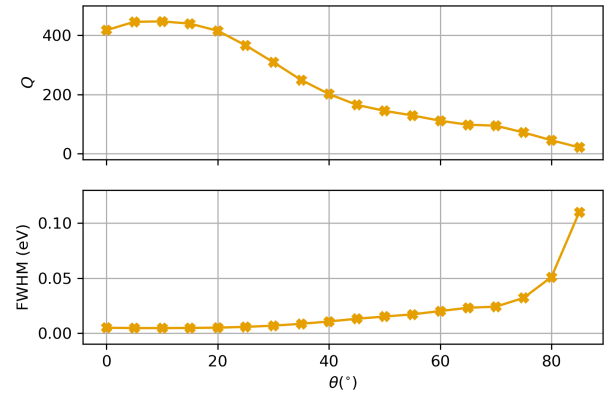

(c)

Fig. 16. In (a), the TE polarized cavity energy as a function of the angle of incidence is shown. The TM polarized energy can be observed at angles of 30° or higher and has slightly lower resonant energies. In (b), the Quality factor and the peak widths (FWHM) to the corresponding cavity energies in (a) are shown.

The quality factor Q, obtains a maximal value of approx. $Q = 500$ between angles of incidence of 5° and 15° which is similar to what others have found for PLD grown oxide microresonators [15]. A theoretical estimate for the quality factor can be given as (rewriting eqn. 32 in terms of the frequency)

$$Q = \frac{\hbar\omega_0}{\hbar\Delta\omega} \tag{40}$$

where $\Delta\omega$, for $1 - R \ll 1$, is given by [16] as

$$\hbar\Delta\omega = \frac{\hbar c(1-R)}{n_c L_{\text{eff}}}. \tag{41}$$

With $R = 0.99$ being the maximal measured value and $L_{\text{eff}} \sim 2650nm$, we get $\hbar\Delta\omega \sim 0.4meV$ and hence a quality factor of $Q \sim 6000$. The large discrepancy between the theoretical and the measured value was also mentioned in [15] and might be due to intra-layer surface roughness between the cavity layer and the Bragg mirrors. Furthermore, the cavity energy at normal incidence differs from the central position of the stop band of the two BR, which would also reduce the reflectivity value R. From Fig. 16, we read off $E_{\text{cav}} = 2$ eV at normal incidence, which gives $R = 0.97$ and hence $Q \sim 2000$. Even though the theoretical maximum is still about four times the measured value, this small correction already shows how sensitive the the quality factor is.

REFERENCES

[1] Maka, Thukela & Chigrin, Dmitry & Romanov, Sergei & Sotomayor Torres, Clivia, 2003, *Three Dimensional Photonic Crystals in the Visible Regime*. 10.2528/PIER0201089e.

[2] P. Yeh, 2005, *Optical Waves in Layered Media*, (New York: Wiley)

[3] A. Kavokin, G. Malpuech, 2003, *Cavity Polaritons*, Elsevier Amsterdam

[4] O. Stenzel, 2005, *The Physics of Thin Film Optical Spectra*, Springer-Verlag Berlin Heidelberg

[5] M S Skolnick et al 1998 Semicond. Sci. Technol. 13 645

[6] A. Grundy, 2009, *Optically Nonlinear Spatial and Spectral Processes in Semiconductor Microcavities*, Dissertation, University of Southampton.

[7] Labcourse Semicoductor Physics, A5: Dielektrische Funktion – Spektroskopische Ellipsometrie.

[8] S. Heiroth, R. Ghisleni, T. Lippert, J. Michler, A. Wokaun, *Optical and mechanical properties of amorphous and crystalline yttria-stabilized zirconia thin films prepared by pulsed laser deposition*, Acta Materialia, Volume 59, Issue 6, 2011, P. 2330-2340, ISSN 1359-6454, https://doi.org/10.1016/j.actamat.2010.12.029.

[9] Michael B. Pomfret, Chad Stoltz, Bindu Varughese and Robert A. Walker, *Structural and Compositional Characterization of Yttria-Stabilized Zirconia: Evidence of Surface-Stabilized, Low-Valence Metal Species*, Analytical Chemistry 2005 77 (6), 1791-1795 DOI: 10.1021/ac048600u

[10] Rémi Boidin, Tomáš Halenkovič, Virginie Nazabal, Ludvík Beneš, Petr Němec. *Pulsed laser deposited alumina thin films*. Ceramics International, Elsevier, 2016, 42 (1, Part B), pp.1177-1182. ff10.1016/j.ceramint.2015.09.048ff. ffhal-01202033f

[11] P. Katiyar, C. Jin, R.J. Narayan, *Electrical properties of amorphous aluminum oxide thin films*, Acta Materialia, Volume 53, Issue 9, 2005, Pages 2617-2622, ISSN 1359-6454, https://doi.org/10.1016/j.actamat.2005.02.027.

[12] H. Tanveer, S. Briesenick, *A5: Spectroscopic Ellipsometry*, Semiconductor Physics I - Laboratory, 2022.

[13] H. Hilmer, C. Sturm, R. Schmidt-Grund, B. Rheinländer, M. Grundmann, *Observation of strong light-matter coupling by spectroscopic ellipsometry*, Superlattices and Microstructures, Volume 47, Issue 1, 2010, Pages 19-23, ISSN 0749-6036, https://doi.org/10.1016/j.spmi.2009.06.007.

[14] Sturm, Chris and Hilmer, Helena and Rheinländer, Bernd and Schmidt-Grund, Rüdiger and Grundmann, Marius, , *Cavity-photon dispersion in one-dimensional confined microresonators with an optically anisotropic cavity material*, Phys. Rev. B, Volume 83, Issue 20, 2011, https://link.aps.org/doi/10.1103/PhysRevB.83.205301.

[15] AIP Conference Proceedings 1199, 151 (2010); https://doi.org/10.1063/1.3295340.

[16] V. Savona, L.C. Andreani, P. Schwendimann, A. Quattropani, Quantum well excitons in semiconductor microcavities: Unified treatment of weak and strong coupling regimes, Solid State Communications, Volume 93, Issue 9, 1995, Pages 733-739, ISSN 0038-1098, https://doi.org/10.1016/0038-1098(94)00865-5.

[17] Dvir Gur, Ben Leshem, Maria Pierantoni, Viviana Farstey, Dan Oron, Steve Weiner, and Lia Addadi, *Structural Basis for the Brilliant Colors of the Sapphirinid Copepods*, Journal of the American Chemical Society 2015 137 (26), 8408-8411 DOI: 10.1021/jacs.5b05289, https://doi.org/10.1021/jacs.5b05289.